Dual fluorine-free salt electrolytes for medium-to-high voltage lithium metal batteries

Journal of Power Sources 667 (2026) 239241

Contents lists available at ScienceDirect

Journal of Power Sources

journal homepage: www.elsevier.com/locate/jpowsour

Dual fluorine-free salt electrolytes for medium-to-high voltage lithium metal batteries

Ashok Kushwaha [a,*], Sayantika Bhakta [a], Mukhtiar Ahmed [a], Andrei Filippov [a], Rong An [b], Patrik Johansson [c,d], Faiz Ullah Shah [a,**]

[a] Chemistry of Interfaces, Luleå University of Technology, SE-971 87, Luleå, Sweden
[b] School of Materials Science and Engineering, Nanjing University of Science and Technology, Nanjing, 210094, China
[c] Department of Physics, Chalmers University of Technology, SE-412 96, Gothenburg, Sweden
[d] Department of Chemistry - Ångström, Uppsala University, SE-751 20, Uppsala, Sweden

HIGHLIGHTS

- Introduces a fluorine-free, flame-retardant dual-salt electrolyte comprising LiSac and LiBOB salts in a TEP solvent.
- The dual salt combination (LiSac and LiBOB) enhances ion transport properties.
- The dual-salt formulation provides effective passivation of the current collectors, and thus suppress the corrosion process.
- The dual salt electrolytes improve the overall electrochemical performance of the LMBs.

ARTICLE INFO

Keywords:
Dual salt
Fluorine-free electrolytes
Lithium saccharinate
Lithium bis(oxalato)borate
Transport properties
Lithium metal battery

ABSTRACT

Flame-resistant and fluorine-free electrolytes based on (combining) the salts lithium saccharinate (LiSac) and lithium bis(oxalato)borate (LiBOB) in a single solvent triethyl phosphate (TEP) solvent and vinylene carbonate (VC) additive are presented and evaluated for lithium metal battery application. The dual salt electrolyte, 1.5 M LiSac + 0.2 M LiBOB in TEP w. 2 % VC, clearly outperforms the single salt ones in terms of electrochemical performance, especially *vs.* $LiNi_{0.8}Mn_{0.1}Co_{0.1}O_2$ (NMC811) cathodes, properties that originate in a Li^+ cation first solvation shell mainly composed of Sac and BOB anions, promoting formation of a mechanically stable, inorganic-rich cathode electrolyte interphase layer, which by X-ray photoelectron spectroscopy was revealed to comprise Li_3N, B_xO_y and SO_3^{2-} species. Overall, this also results in stable cycling, and a capacity retention of 86 % in both Li||$LiFePO_4$ and Li||NMC811 cells after 500 cycles at 1C rate – hence offering an intrinsically safer electrolyte that also enables the use of both lithium metal anodes and medium-to-high-voltage cathodes.

1. Introduction

With the rapidly increasing demand for high energy density batteries, lithium metal batteries (LMBs) have been extensively pursued [1,2]. Lithium metal anodes offer a high specific capacity of 3860 mAh g^{-1}, a low redox potential of −3.04 V *vs.* SHE, and a low gravimetric density of 0.534 g cm^{-3} [3,4]. To match the high specific capacity of lithium metal and truly develop high energy density LMBs various medium-to-high-voltage advanced cathodes have been explored and commercialized [5,6]. However, despite the many promising features of LMBs and the enormous progress made, the electrolytes employed are still most often based on fluorinated lithium salts and flammable carbonate-based solvents [7,8]. In addition, these electrolytes are incompatible with lithium metal, as they promote dendrite growth, side reactions, and dead lithium formation, resulting in low coulombic efficiency and potential thermal runaway [9,10].

Solid-state electrolytes (SSEs), in particular garnet- and sulfide-based SSEs [11,12], hold large promise due to their enhanced safety, great compatibility with lithium metal, and potential to achieve high energy densities [13–15]. However, drawbacks include high mechanical stiffness – rendering poor interfacial contact with lithium and problems of cell relaxation during cycling demanding (high) external pressure to be

* Corresponding author.
** Corresponding author.
E-mail addresses: ashok.kushwaha@associated.ltu.se (A. Kushwaha), faiz.ullah@ltu.se (F.U. Shah).

https://doi.org/10.1016/j.jpowsour.2025.239241
Received 24 October 2025; Received in revised form 8 December 2025; Accepted 29 December 2025
Available online 2 January 2026

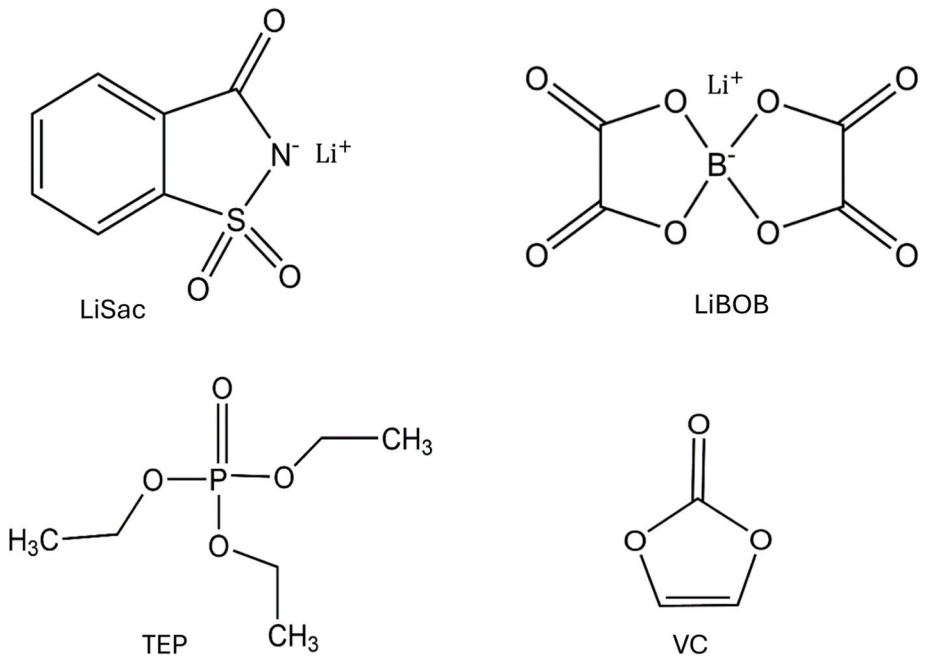

Fig. 1. Chemical structures of LiSac, LiBOB, TEP, and VC.

applied, high cost of production, and low ionic conductivity at room temperature [13,16]. Solid polymer electrolytes (SPEs) have been explored, being mechanically flexible, less dense, less costly, and easier to process [17,18], but SPEs suffer from low ionic conductivity at room temperature and most often limited interfacial stability *vs.* lithium metal [18,19].

Hence, liquid electrolytes continues to be a main route forward for LMBs [20]. The lack of safe yet high-performant liquid electrolytes is, however, one of the main challenges for LMB with some notable work focusing on flame-retardant solvents and fluorine-free salts [21–27]. The main challenges of fluorine-free electrolytes are how to form both a robust solid electrolyte interphase (SEI) on the anode and likewise cathode electrolyte interphase (CEI) on the cathode, as well as passivating the Al current collector [28,29]. As for now fluorine-free salts and flame-retardant solvents are typically employed as additives [25,30,31]. Some examples of such solvents are ionic liquids [32], organosilicon compounds [33], fluoroethers [34], and phosphate-based solvents [35], such as triethyl phosphate (TEP), trimethyl phosphate (TMP), and diethyl ethyl phosphonate (DEEP). The phosphate-based solvents possess high donor numbers (DNs), enabling efficient dissolution and dissociation of lithium salts, and they also offer low cost along with high oxidative and thermal stability [31,36,37].

As for fluorine-free lithium salts, typical alternatives are lithium bis (oxalato)borate (LiBOB), lithium nitrate ($LiNO_3$), lithium tricyanomethanide (LiTCM), lithium dicyanamide (LiDCA), and lithium (1-naphthalenesulfonyl)-dicyanomethide (LiNPDM), *etc*. [38–42] Looking at the former, LiBOB based electrolytes are characterized by minimal hazardous decomposition and better thermal stabilities than those based on $LiPF_6$ and can also create stable SEIs [43,44]. LiBOB has been reported to create stable CEI layers containing borate species, which can prevent electrolyte oxidation and protect against HF attacks at high voltages in LMBs. In addition, these CEIs can reduce the formation of the Li_2MnO_3 phase, capture active oxygen from the NMC cathode surface, and furthermore also passivate aluminum current collectors [45–47]. However, the limited solubility of LiBOB in carbonate solvents and the relatively lower ionic conductivity of its electrolytes restrict its use to an additive rather than as a primary electrolyte salt [30]. In addition, BOB is prone to hydrolysis and decomposes upon exposure to moisture [48].

To resolve these problems but still be able to use a non-fluorinated salt, we look towards dual salt electrolytes, and keeping LiBOB we do need a suitable co-salt. Our group has previously reported on the synthesis and characterization of lithium saccharinate (LiSac) based electrolytes [49], demonstrating that this salt can be synthesized via a simple and green approach, yielding products with high electrochemical and thermal stability, and exhibits structural and chemical property similarities to fluorinated salts, such as lithium bis(trifluoromethanesulfonyl)imide (LiTFSI) and lithium (2,2,2-trifluoro-*N*-(trifluoromethylsulfonyl)acetamide (LiTSAC) [49–51].

As for the concept of dual salt electrolytes, these can indeed improve both the SEI and CEI, and also prevent dendrite formation and growth [52,53]. Zheng et al., Miao et al., and Jian et al. have all reported that dual salt electrolytes can form denser and thinner interphases, effectively suppress side reactions and dendrite formation, while also improving oxidation stability and electrochemical cycling performance [54–56]. Yet, most electrolyte designs still need at least one additive. Among fluorine-free electrolyte additives, vinylene carbonate (VC) is widely studied and known to serve in the formation of stable and functional SEIs. Furthermore, it polymerizes at the cathode, suppressing side reactions and also slightly improving the kinetics, due to its preferential reduction prior to that of *e.g.* TEP [31,57].

In addition, the presence of VC in the electrolytes brings the reduction species that help in the formation of a homogeneous and stable SEI layer [58].

Based on all of the above, we here present a flame-resistant and fluorine-free dual salt electrolyte using TEP as solvent, LiSac as the primary salt and LiBOB as the secondary salt, and VC as additive (Fig. 1). For comparison, electrolytes based on the individual salts in the same solvent are also evaluated with respect to electrochemical performance, such as cycling stability and rate capability, with special attention to CEI composition and stability in LMB cells.

2. Experimental

2.1. Electrolyte and electrode preparation

The details of synthesis and characterization of LiSac are given elsewhere [49]. Prior to use, LiSac and LiBOB (Sigma Aldrich, ≥99.9 % trace metals basis) were both dried in a vacuum oven at 120 °C for 24 h,

followed by transferring to an argon-filled glovebox (O_2 and $H_2O < 0.5$ ppm) and then dissolved in a dried (48 h in 4 Å-molecular sieves (Sigma Aldrich, beads, 4–8 mesh)) TEP (Sigma Aldrich, ≥99.8 %) and 2 vol% VC (Sigma Aldrich, battery grade, ≥99.5 %) solvent mixture, to create differently concentrated electrolytes (Table S1). The water content of the electrolytes is < 40 ppm as determined by a Metrohm 917 Coulometric Karl Fischer titrator. The benchmark electrolyte, 1.0 M $LiPF_6$ in ethylene carbonate (EC)-dimethyl carbonate (DEC) (LP40, EC:DEC = 50:50 vol:vol., Sigma-Aldrich, battery grade), was used as received.

The positive electrode was fabricated using Doctor blading. Lithium iron phosphate (LFP), (Guangdong Canard New Energy Technology Co., Ltd, China) served as the active material, while Super P carbon black (Thermo Fisher chemicals, >99 %, metal basis) was employed as a conductive agent, and polyvinylidene fluoride (PVdF) (Sigma Aldrich, average M_w ~530,000) was used as the binder, with a mass ratio of 80:10:10. *N*-methyl-2-pyrrolidone (NMP) (Sigma Aldrich, ACS reagent, ≥99.0 %) was used as the solvent. The same methodology was applied to prepare electrodes using $LiNi_{0.8}Mn_{0.1}Co_{0.1}O_2$ (NMC811; Guangdong Canard New Energy Technology Co., Ltd, China). The resulting electrodes were dried in a vacuum oven at 90 °C for 12 h and subsequently punched into circular discs with a diameter of 14 mm. The mass loading of the prepared electrodes was approximately 2.5 mg cm^{-2}.

2.2. Ionic conductivity

The ionic conductivity was measured by impedance spectroscopy within a frequency range from 1 Hz to 1 MHz, using an AC voltage amplitude of 10 mV_{rms}. The measurements were carried out using both heating and cooling cycles over a temperature range of −20 to 40 ± 0.1 °C. A two-electrode setup was employed, utilizing a platinum wire as the working electrode (WE) and a 70 μL platinum crucible serving as both the sample container and the counter electrode (CE). To ensure consistency, the cell was thermally stabilized for 10 min before each measurement. Both the electrodes were polished with 0.25 μm Kemet diamond paste before each experiment, and the cell constant was calibrated using a Metrohm 100 μS cm^{-1} KCl standard solution (κ_{cell} = 18.002 cm^{-1}).

The relationship between ionic conductivity (σ) and temperature (*T*) was modeled using the Vogel–Fulcher–Tammann (VFT) equation (Equation (1)); σ_0 represents the pre-exponential factor, B and T_0 are adjustable parameters, and R denotes the gas constant. B is related to the glass transition temperature (T_g) and the activation energy (E_σ), where $E_\sigma = B^*R$, whereas T_0 corresponds to the ideal glass transition temperature, signifying the point at which the configurational entropy approaches zero.

$$\sigma = \sigma_0 \exp\left(\frac{-B}{(T - T_0)}\right) \quad (1)$$

2.3. NMR diffusometry

A Bruker Ascend Aeon WB 400 (Bruker BioSpin AG) nuclear magnetic resonance (NMR) spectrometer with an operating frequency of 400.21 MHz for ^1H, 155.56 MHz for ^7Li and 128.40 MHz for ^{11}B was used, alongside a Diff50 Pulsed-Field-Gradient (PFG) NMR probe (Bruker). The greatest magnetic field gradient pulse amplitude was 29.73 T m^{-1}. Samples were placed in a standard 5 mm NMR glass tube and given at least 20 min to equilibrate at each temperature before experiment.

A molecule's diffusivity is measured by the diffusion decay (D) of the amplitude (A) of the NMR spectral line, which is obtained by Fourier transforming the descending half of the stimulated echo (StE). This decay, as a function of the amplitude of the applied pulsed field gradient, can be described by Equation (2) for a basic non-associating molecular liquid under the utilized stimulated echo pulse sequence:

$$A(g, \delta, t_d) = A(0)\exp\left(-\gamma^2 g^2 \delta^2 D t_d\right) \quad (2)$$

Here, A(0) denotes the factor proportional to the system's proton concentration, as well as the spin-lattice and spin-spin relaxation durations. A is the integral intensity of the NMR signal, τ and τ1 are time intervals in the pulse train; g is the gyromagnetic ratio for magnetic nuclei; g and δ are the amplitude and length of the gradient pulse; $t_d = (\Delta - \delta/3)$ is the diffusion time; and $\Delta = (\tau + \tau 1)$. D represents the diffusion coefficient. The measurements ranged from 1 to 3.0 ms for δ, 3.0–5.0 ms for τ, and 0.06–29.73 T m^{-1} for g. The diffusion time (t_d) ranged from 20 to 100 ms. The recycling latency during signal transient accumulation was 5 s.

The diffusivity data were analyzed by fitting to the following VFT Equation (3):

$$D = D_0 \exp\left(\frac{-B}{(T - T_0)}\right) \quad (3)$$

where D_0, T_0, and *B* are adjustable parameters. The activation energy for diffusion (E_D) relate to *B* as $E_D = B \times R$. We have described $D(T)$ by fitting D_0, T_0, and *B*. The apparent transference numbers (t_i) for each ion in the dual salt electrolyte were calculated from their diffusion coefficients using Equation 4 [59,60]:

$$t_i = \frac{x_i D_i}{\Sigma_i x_i D_i} \quad (4)$$

where t_i is the apparent transference number, x_i is the molar fraction of each individual ion, and D_i is the self-diffusion coefficient of the ion.

2.4. FTIR spectroscopy

For the Fourier transform infrared (FTIR) spectroscopy, attenuated total reflection (ATR-FTIR) spectra were recorded using a Bruker IFS 80v spectrometer. The instrument had a deuterated triglycine sulfate (DTGS) detector and a diamond ATR accessory, operating in the double-side forward-backward acquisition mode. The spectra were obtained with a total of 64 scans, co-added, and signal-averaged, at an optical resolution of 4 cm^{-1}.

2.5. Electrochemical assessments

The electrochemical performance was evaluated using CR2032 coin cells with glass fiber separators (Whatman, grade GF/D, diameter 18 mm, thickness 0.67 mm) and 120 μl of electrolyte. Galvanostatic charge-discharge cycling was conducted for the LFP cells within a voltage range of 2.5–4.0 V and for the NMC811 cells within 2.8–4.3 V. Symmetric Li||Li cells were prepared using a lithium metal sheet (0.45 mm, TMAX Ltd., Xiamen, China), with cut-outs at a diameter of 14 mm. The Li||Cu half cells were assembled using a polyethylene (PE) separator (38 μm, TMAX Ltd., Xiamen, China). Prior to cell assembly, copper foil was pretreated to remove its naturally formed oxide layer through the following steps: (1) a 1.0 M HCl solution was prepared in deionized (DI) water, and the copper foil was immersed in the solution for 1 min, (2) the acid-treated copper foil (9 μm, Cambridge Energy Solution) was then wiped with lint-free tissue paper, thoroughly rinsed with deionized water and acetone multiple times, and (3) the cleaned copper foil was dried in a vacuum oven at 60 °C for 12 h. For cell preparation, the treated copper foil was cut to a diameter of 16 mm, while lithium metal was cut to a diameter of 14 mm. Prior to assembly, the copper foil was rinsed with dichloromethane and stored in an argon-filled glovebox.

The coulombic efficiency was determined by conducting initial cycles within a potential range of 0–1.0 V at a current density of 0.1 mA cm^{-2}. Subsequent cycling was performed at a current density of 0.5 mA cm^{-2} with a capacity of 1.0 mAh cm^{-2} at 1.0 V. All these electrochemical measurements were performed using BCS and VMP3 electrochemical workstations (Biologic).

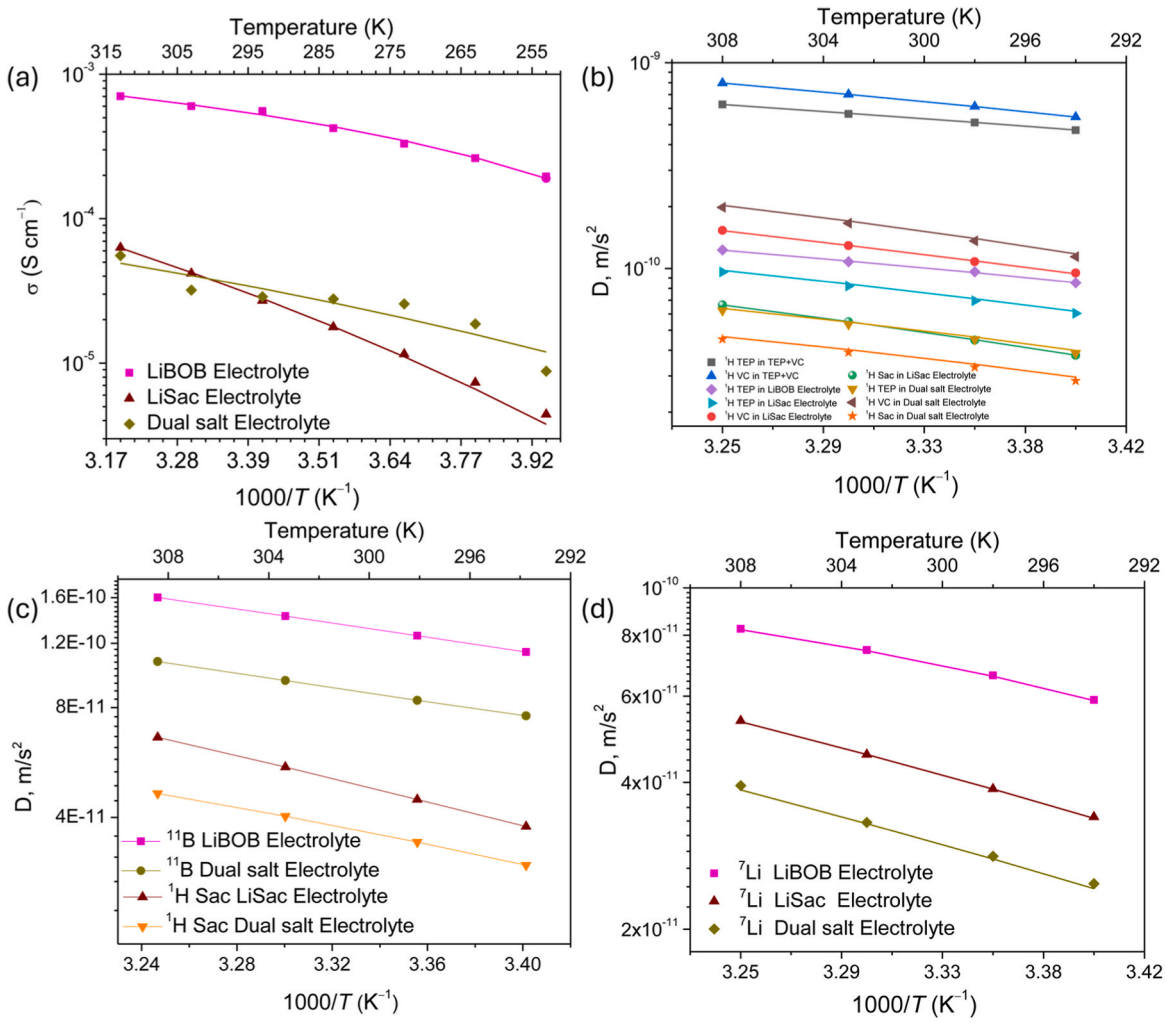

Fig. 2. Ionic conductivity as a function of temperature (a) and diffusion coefficients by ^{1}H (b), ^{1}H and ^{11}B (c), and ^{7}Li (d) NMR diffusometry. The symbols indicate experimental data, and the solid lines represent the VFT fits.

The corrosion tests were performed using an Autolab (Metrohm) electrochemical workstation. Before each test, an aluminum current collector was cleaned using ultrasonication in deionized water and acetone for 5 min. The corrosion resistance of the aluminum current collector (20 μm, Cambridge Energy Solution) was evaluated using cyclic voltammetry (CV), linear sweep voltammetry (LSV), and potentiodynamic polarization techniques. CV and LSV measurements were performed in the potential range from 2.0 to 5.0 V and from 3.0 to 6.0 V at a scan rate of 1 mV/s. A potentiodynamic polarization test was conducted by applying a potential range of 1.0–5.0 V at a scan rate of 5 mV/s. In addition, chronoamperometry was conducted using Li||Al cells at different potentials (at 3.5, 4.0, 4.3, 4.5, and 5.0 V vs. Li/Li^{+}) for 10 h.

The transference numbers (t_{Li+}) were evaluated using the Bruce-Vincent method [61] as described by Abraham et al.: [62] The initial (I_0) and steady-state (I_{ss}) DC polarization currents were measured by applying a small perturbation potential (ΔV) of 10 mV using Li/Li symmetric cells. Correspondingly, before and after the polarization test, initial and steady-state bulk resistances (R_{b0} and R_{bss}) and interfacial resistances (R_{i0} and R_{iss}) were examined via electrochemical impedance spectroscopy (EIS). Equation (5) was then used to calculate t_{Li+} as:

$$t_{Li+} = \frac{I_{ss}(\triangle V - I_0 R_{i0})}{I_0(\triangle V - I_{ss} R_{iss})} \quad (5)$$

2.6. Surface analyses

Scanning electron microscopy (SEM, FEI Magellan-400) operating at an acceleration voltage of 3 kV and a fixed working distance of ~5.4 mm, was used to examine the morphology of the Al current collectors after the corrosion/passivation tests. To investigate the formation and structure of the CEI on the NMC811 electrode after electrochemical cycling, X-ray photoelectron spectroscopy (XPS) was performed using a PHI QUANTERA II spectrometer equipped with a monochromatic Al Kα X-ray source (1486.6 eV) and a pass energy of 30 eV. The surface composition was examined based on the recorded spectra, which were calibrated by referencing the C-C peak to a binding energy of 284.8 eV. Prior to XPS analysis, the cycled NMC811 electrodes were rinsed three times with dimethyl carbonate (DMC) solvent to remove any residual salt and subsequently dried in an argon-filled glovebox. Since our focus is on the stability of the CEI and SEI and their role in enabling medium-to high-voltage LMBs, the CEI composition was analyzed using XPS, while the SEI morphology on copper foil after plating/stripping cycles was evaluated by SEM. To avoid exposure to ambient conditions, however, all the electrode samples were sealed within the glovebox prior to XPS and SEM analysis.

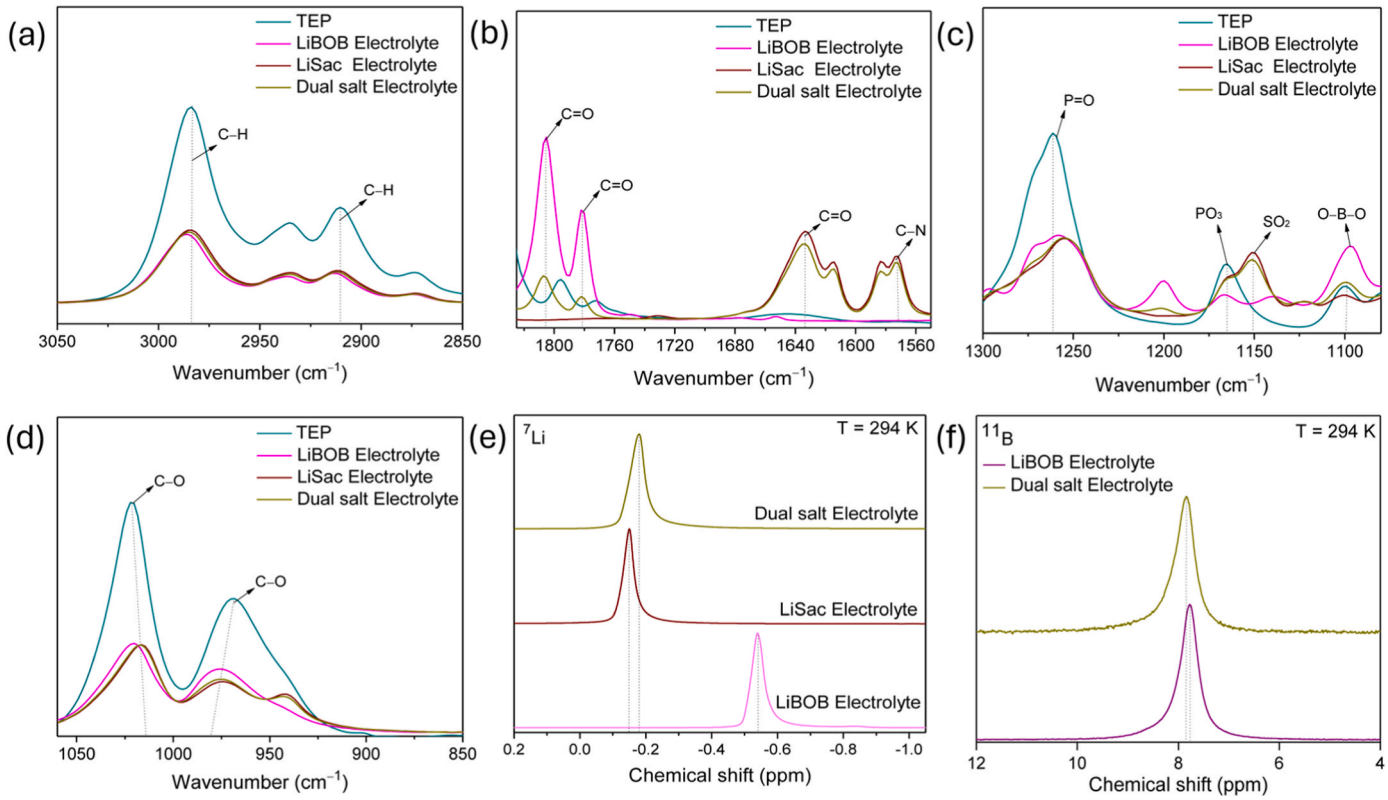

Fig. 3. FTIR spectra of some selected spectral regions (a–d), and ^{7}Li (e) and ^{11}B (f) NMR spectra of the electrolytes.

3. Results and discussion

We begin by briefly describing the design and formulation of the electrolytes, especially the solubility of the LiSac and LiBOB salts, followed by a systematic investigation of key transport properties, including ionic conductivity, ion diffusion, and ion interactions, using FTIR and NMR spectroscopy. Thereafter, corrosion of aluminum current collectors is reported upon as well as the compatibility with lithium and copper metal foils. Finally, the electrochemical performance of the dual salt electrolyte in Li||LFP and Li||NMC811 cells is reported upon, which is supplemented with surface analysis of the NMC811 electrode to elucidate the CEI details and SEI morphology on copper foil study after plating/stripping and correlating with practical LMB cell performance.

3.1. Electrolyte design and formulation

Many lithium salts present challenges in terms of solubility in organic solvents, and generally, solvents with high donor numbers (DNs) have been used to address these challenges by promoting interactions between the salt cation and the solvent(s). Both LiSac and LiBOB have low solubilities in the commonly studied carbonate-based solvents, due to strong electrostatic interactions between Li^+ and the anions, but using TEP, with its high DN (26 kcal mol^{-1}), facilitates salt dissolution [63]. Two single salt electrolytes, 1.0 M LiBOB and 1.5 M LiSac, and one dual salt electrolyte, 1.5 M LiSac + 0.2 M LiBOB, are reported on here. The latter was found to be the optimal dual salt electrolyte composition; less concentrated electrolytes, for example 1.0 M LiSac + 0.1 M or 0.2 M LiBOB, did not provide adequate cycling stability of Li||LFP cells (Fig. S1).

The electrolytes exhibit transparent and clear solutions, even at rather high concentrations of LiSac (Fig. S2). In contrast, LiBOB was limited in solubility to *ca.* 1.0 M (Fig. S3), and this is why our comparative studies used a 1.0 M LiBOB electrolyte. Overall, the electrolyte design and formulation is based on the following assumption: The dual salt electrolyte comprising Sac and BOB anions act synergistically; the Sac anion to regulate the Li^+ cation first solvation shell, reducing the desolvation energy, while the BOB anion to increase the ionic conductivity and promote formation of robust inorganic-rich SEI and CEI layers, combined leading to the observed improved kinetics and stabilities of both Li||NMC811 and Li||LFP cells [47,64].

As a side-note, but an important such, these electrolytes display much better thermal stabilities and being flame-resistant, even when ignited continuously for a longer period, as compared to the benchmark LP40 electrolyte (Figs. S4–6).

3.2. Transport properties

Starting with the ionic conductivities, the single salt LiBOB electrolyte performs the best overall and the LiSac electrolyte the worst, but most notably the dual salt electrolyte displays higher ionic conductivities than the single salt electrolytes at lower temperatures, while it aligns with the former at higher temperatures (Fig. 2a). In addition, the LiBOB electrolyte exhibits the lowest E_a and the LiSac electrolyte the highest, with the dual salt electrolyte landing intermediate (Table S2). The multinuclear (^{1}H, ^{7}Li, and ^{11}B) NMR diffusometry showed that regardless of the electrolyte composition, the TEP solvent diffuses the fastest, followed by the anions, while the Li^+ cation diffuses the slowest (Fig. 2b–d), and VC diffuses even slightly faster than TEP. Comparing the mobilities of ionic species within the three electrolytes, the BOB anion diffuses much faster in the single salt LiBOB electrolyte than the dual salt one. Similarly, the Sac anion diffuses faster in the single salt LiSac electrolyte than in the dual salt electrolyte. Comparing the diffusivity of BOB and Sac anions within the dual salt electrolyte, the former diffuses than the latter, indicating weak interactions with the Li^+ cation.

As in the case of ionic conductivity data, Li^+ cation diffuses much faster in the single salt LiBOB electrolyte, followed by the LiSac electrolyte, and much slower in the case of the dual salt electrolyte. The diffusion coefficients of the ionic species in the dual salt electrolyte are

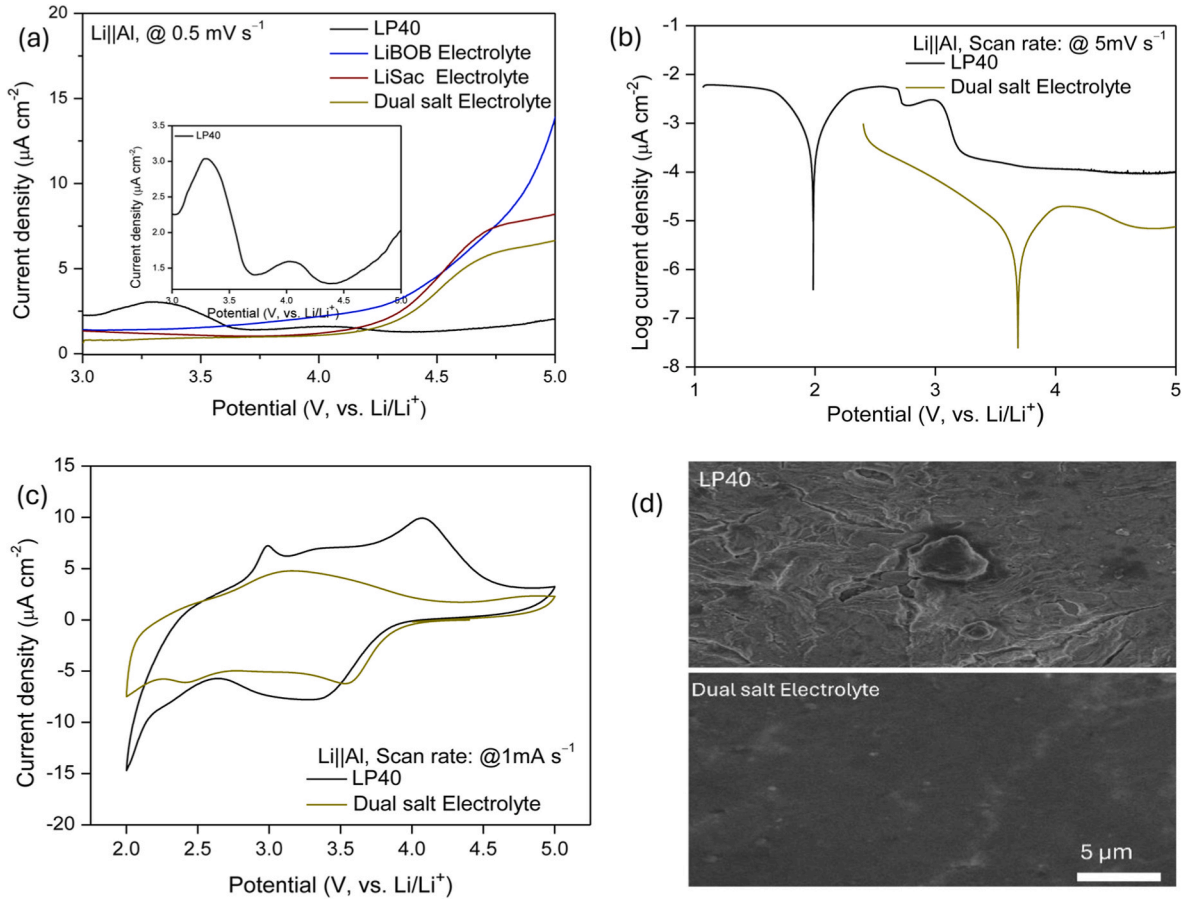

Fig. 4. Corrosion/passivation of the Al current collector using Li||Al cells: (a) LSV curves, (b) Tafel plots, (c) CVs, and (d) SEM images.

in general smaller than for the single salt electrolytes, indicating that increasing salt concentration leads to increased ion-pairing/aggregation, and more importantly, the ion transport in highly concentrated electrolytes can proceed via other mechanisms not probed by the diffusion coefficient [65,66]. However, the ion aggregate are readily dissociated with increasing temperature, as evident from both the ionic conductivity and diffusion data.

3.3. Ion-ion and ion-solvent interactions

FTIR and liquid state (^{7}Li and ^{11}B) NMR spectroscopies, employed to investigate ionic interactions and the cation solvation, first of all show that the FTIR bands at 2984 cm^{-1} and 2910 cm^{-1} of TEP have minor shifts toward lower wavenumbers for all electrolytes, suggesting interaction with Li^+ (Fig. 3a). The single salt LiBOB-based electrolyte exhibits two strong bands at 1804 and 1781 cm^{-1} attributed to the carbonyl groups (Fig. 3b) [67,68]. For the LiSac-based single and dual salt electrolytes, the Sac C=O band at 1635 cm^{-1} exhibits symmetric features with a shoulder, indicating symmetry-induced splitting [69,70]. The band at 1153 cm^{-1} with a shoulder at higher wavenumbers is due to the SO_2 group of the Sac anion (Fig. 3c). As these vibrations do not change, the addition of LiBOB does not influence the Sac anion interactions. For TEP, the P−O bands at 1261 cm^{-1} and 1165 cm^{-1} [71] shift slightly upon salt addition as well as the C−O bands at 1021 cm^{-1} and 969 cm^{-1} that shift to 1017 cm^{-1} and 974 cm^{-1}, respectively [72].

Turning to the NMR spectroscopy, the ^{7}Li NMR spectra reveal single resonance lines that for both the single and dual salt LiSac-based electrolytes are shifted slightly downfield (by *ca.* 0.3 ppm) as compared to the single LiBOB-based electrolyte (Fig. 3e). This suggests that the Li^+ cation experiences less shielding in the presence of the Sac anion, in contrast to the LiBOB-based electrolyte, with many anions in the cation first solvation shell and hence stronger ion-pair interactions [63,73]. Furthermore, the ^{11}B NMR spectra of the LiBOB-based and the dual salt electrolytes both reveal single resonance lines, the latter shifted slightly downfield (Fig. 3f). The slight de-shielding of ^{11}B NMR spectrum together with the shielding of ^{7}Li NMR spectrum confirms that incorporating 0.2 M LiBOB into the 1.5 M LiSac electrolyte changes the strength of ion–solvent interactions, thereby improving the reduction stability of the electrolyte and enabling the formation of a robust interfacial layer on the electrodes.

3.4. Corrosion/passivation of aluminum current collectors

The oxidation stability evaluation using LSV and a Li||Al cell configuration shows a high current density for the single salt LiBOB electrolyte at 4.3 V *vs.* Li/Li^+, indicating inefficient passivation (Fig. 4a). In contrast, the 1.5 M LiSac-based electrolyte has a flatter response up to 4.3 V and beyond that a much lower current density, suggesting effective passivation, and the dual salt electrolyte behaves similarly. The passivation of the Al current collectors was further analyzed through chronoamperometry (Fig. S7). The dual-salt electrolyte shows stable passivation and minimal leakage current up to 4.3 V and displays comparable behavior to the LP40 electrolyte at higher voltages. Although fluorinated electrolytes are known to passivate by the formation of Al–O–F compounds, $LiPF_6$ and LiTFSI based electrolytes are also prone to corrode Al current collectors at higher potentials.

Another possible contributor to corrosion is EC-based solvents [74]. As these solvents oxidize at higher potentials, they produce protons, which can react either directly with the Al surface or with anions to produce reactive species. In Fig. 4a, the inset graph for LP40 shows the

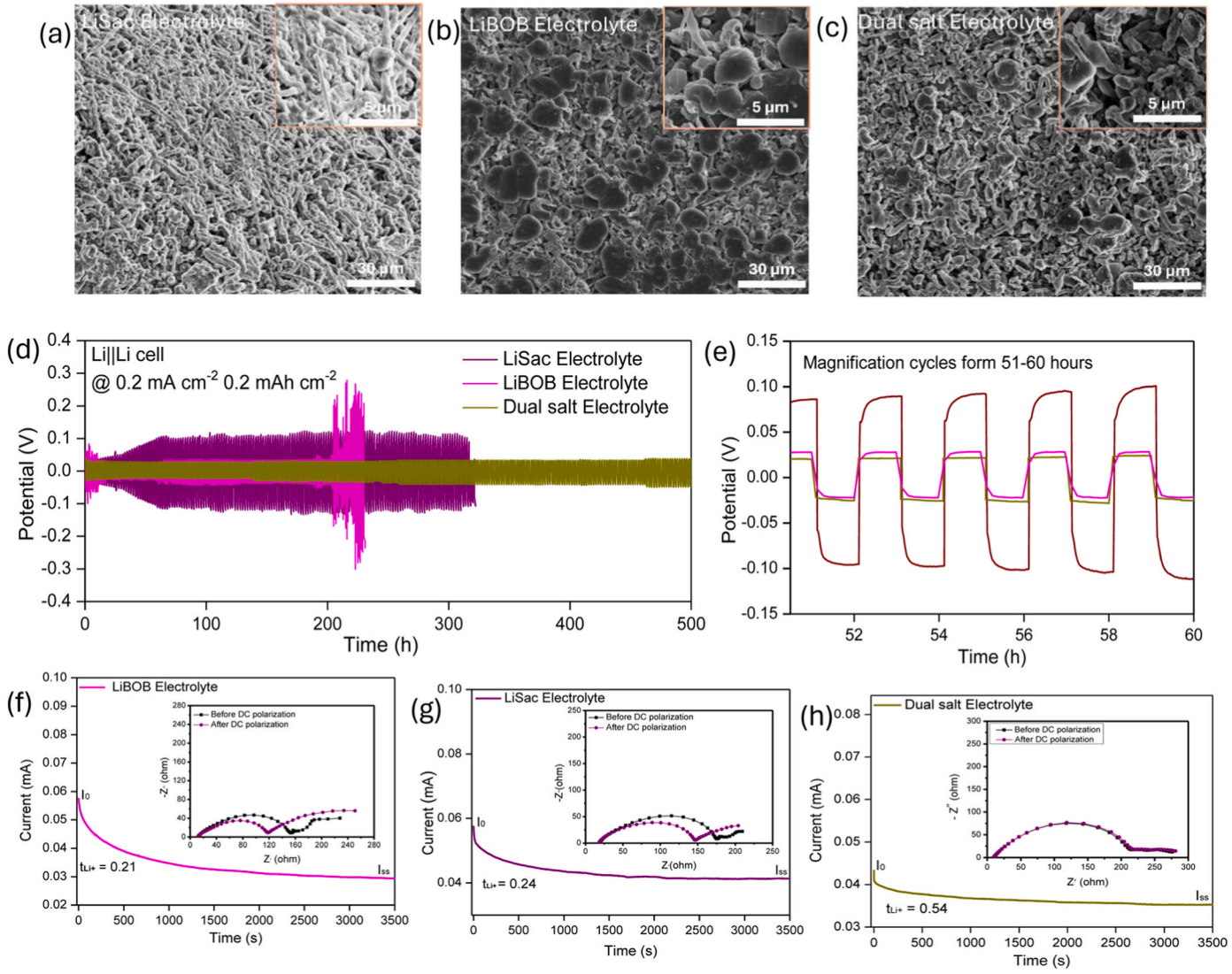

Fig. 5. SEM images of the cycled copper foils after 15 plating/stripping cycles at a current density of 0.2 mA cm^{-2}, using the LiSac (a) LiBOB, (b), and dual salt electrolytes (c). Galvanostatic cycling of Li||Li symmetric cells at 0.2 mA cm^{-2} current density (d), and magnified data for 51–60 h (e). Chronoamperometry DC polarization graph and EIS spectra before and after DC polarization test (inset) of cells with single salt electrolytes (f and g) and the dual salt electrolyte (h).

formation of passivation layers at lower potentials and signs of corrosion or solvent oxidation at higher potentials. As a second assessment, the Tafel polarization plot using Li||Al cells reveals both a higher corrosion potential and a lower corrosion current density for the fluorine-free dual salt electrolyte, demonstrating that it effectively mitigates the corrosion of the Al current collectors and clearly outperforms the LP40 electrolyte (Fig. 4b).

Turning to the CVs, the LP40 electrolyte CV displays an oxidation current peak at low potential (Fig. 4c), which indicates passivation of the current collector, by the following process, Al → Al^{3+}(ad) + $3e^{-}$, Al^{3+}(ad) + anion/solvent → Al^{x+} – complex(ad), while the higher potential peak is associated with electrolyte oxidation or surface/pit corrosion [75–77]. In stark contrast, no sharp oxidation peaks are observed in the dual salt electrolyte CV. This suggests that the dual-salt electrolyte creates a compact passivation layer on the aluminum surface through the incorporation of Al^{3+} and B–O compounds, and thus effectively reduces surface oxidation. Notably, fluorine-free salts such as LiBOB cannot produce species such as hydrogen fluoride (HF), and thereby they enhance the stability under high-voltage conditions [78]. This is further confirmed by our SEM analysis showing the former surface to exhibit various clear pits and cavities, and the latter no such features whatsoever (Fig. 4d).

3.5. *Electrochemical performance*

Starting with the compatibility *vs.* Li and Cu surfaces, there is a significantly improved stability of the Li plating/stripping processes when using the dual salt electrolyte as compared to both the LP40 and single salt electrolytes (Fig. S8a), suggesting stability of the electrolyte and no side-reactions with lithium metal. Yet, the Coulombic efficiency (CE) is only ~84 % after 150 cycles. The dual salt electrolyte thus shows better performance than the LP40 electrolyte, but the CE remains relatively low as compared to when using other, for LMBs optimized, fluorinated electrolytes [79]. The initial voltage profiles (Fig. S8b) suggest that the cell with the dual salt electrolyte exhibits an initial CE of *ca.* 75 %, closely matching the 78 % of that using the LP40 electrolyte, pointing to that the addition of the BOB anion enhances the reversibility of the Li plating/stripping processes [80], and furthermore also improves the lithium transfer kinetics as seen in the Tafel plots of the symmetric Li||Li cells (Fig. S8c).

Moreover, the interfacial resistance of the lithium metal electrodes was evaluated by EIS after Li plating/stripping using Li||Li symmetric

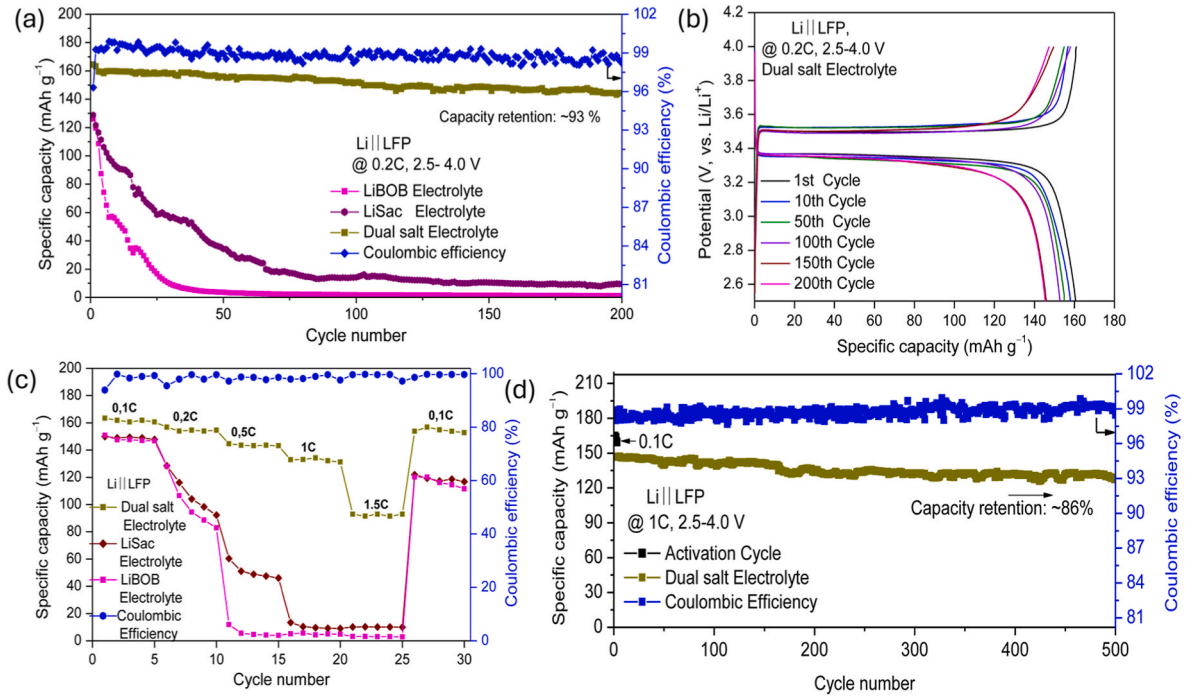

Fig. 6. Galvanostatic cycling of Li||LFP cells at 0.2C rate (a). Corresponding charge-discharge curves for the cell using the dual salt electrolyte (b). Rate performance from 0.1C to 1.5C and back to 0.1C (c). Galvanostatic cycling at 1C rate (after 3 cycles of conditioning at 0.1C) (d).

cells (Fig. S9) showing the cells with the single salt electrolytes to exhibit high interfacial resistances before cycling and then decreasing progressively with cycling, which we attribute to an unstable SEI. In contrast, the dual salt electrolyte demonstrates a higher initial interfacial resistance, which only slightly decreases upon cycling, suggesting the formation of a stable SEI. Furthermore, the dual salt electrolyte exhibits the highest current response using Li||Cu cells, confirming enhanced kinetics (Fig. S8d). Notably, the cells with single salt electrolytes show rather similar current responses, but higher lithium plating overpotentials. Additionally, the top-view morphology of the cycled copper foils reveals that the LiSac-based electrolyte results in a fibrous, thread-like growth and a porous structure. In contrast, the LiBOB based electrolyte leads to the formation of larger, non-uniform lithium particles deposition, indicating that the single fluorine-free salt electrolyte is ineffective in the formation of a stable SEI, as well as in preventing the formation of dendrites and dead lithium (Fig. 5a and

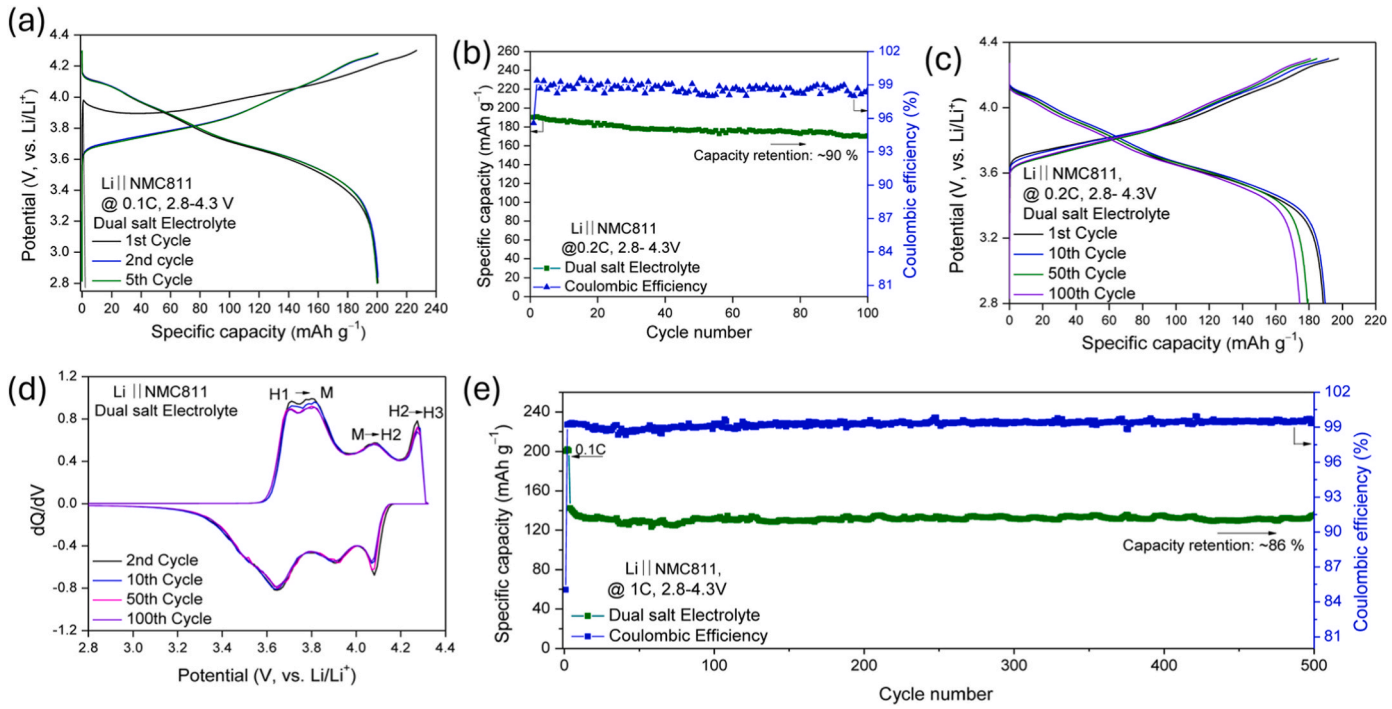

Fig. 7. Charge-discharge curves of Li||NMC811 cell at 0.1C rate (a). Galvanostatic cycling at 0.2C rate (b), the corresponding charge-discharge curves of the Li||NMC811 cell (c), and associated dQ/dV plot (d). Galvanostatic cycling at 1C rate (after 3 cycles of conditioning at 0.1C) using the dual salt electrolyte (e).

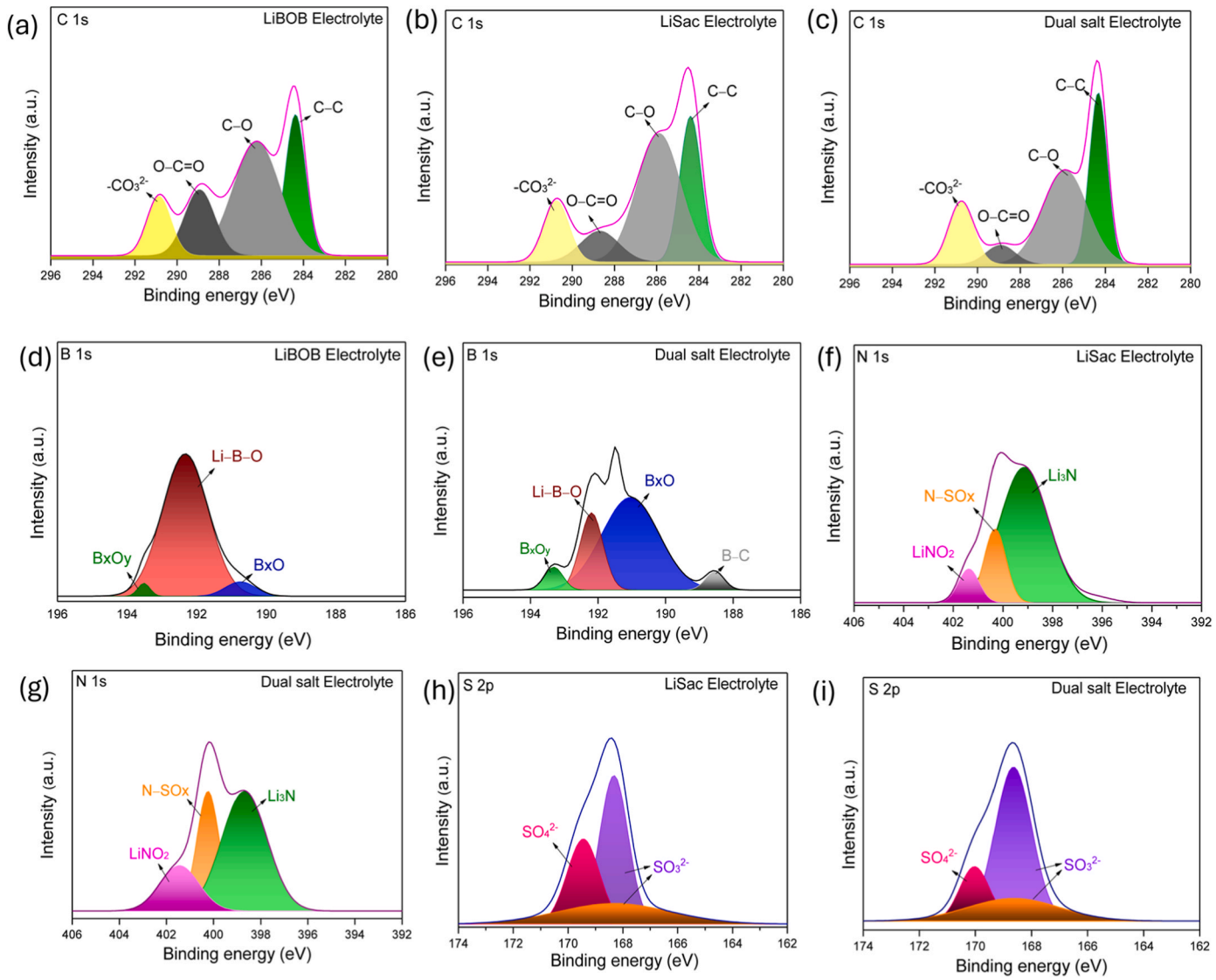

Fig. 8. XPS C1s spectra of the CEI of NMC811 after 50 cycles at 0.2C rate using the fluorine-free electrolytes (a–c). The deconvoluted C 1s spectral components corresponding to the data points are presented in Table S5 B 1s spectra (d, e), N 1s spectra (f, g), and S 2p spectra (h, i).

b). On the other hand, the dual-salt electrolyte produces smaller lithium deposits; the nucleation remains non-compact, suggesting that dendrite growth and dead lithium still occur during the initial plating/stripping cycles in Li||Cu cells (Fig. 5c).

The galvanostatic cycling of the Li||Li symmetric cells show the LiBOB-based electrolyte to have the higher initial polarization potential, which fluctuates for a few cycles before stabilizing at lower polarization (Fig. 5a). However, after 112 cycles the polarization increases again and quite drastically so, most likely due to the side reactions, dead lithium formation, and/or dendrite growth [81–83] most likely the former as dendrite growth under these low current densities is unlikely, and hence the polarization most probably is due to continuous electrolyte decomposition and growth of a thick, resistive SEI. In contrast, the cell with the LiSac-based electrolyte exhibits a similar initial polarization potential, which fast increases gradually and stabilizes at ±0.13 V, while the cell with the dual salt electrolyte shows a lower polarization potential of ±0.08 V, which only slightly increases as it stabilizes. The magnified view further highlights the superior stability of the latter cell (Fig. 5b).

The lithium-ion transference numbers (t_{Li+}) are determined both by using PFG NMR diffusometry and by using chronoamperometry DC polarization graphs and the Bruce–Vincent method (Fig. 5c–e). The latter renders the dual salt electrolyte a much higher t_{Li+} (0.54) as compared to the single salt electrolytes, which is in reasonable agreement with the value calculated from the diffusion data (0.42) (Table S4). Hence, although the single salt LiBOB-based electrolyte displays higher ionic conductivity (Fig. 2a), the dual salt electrolyte is likely more functional, with a Li^+ transference number both higher than, *e.g.* LP40 (0.31) [84] and comparable to fluorinated dual salt electrolytes (0.49–0.83) [85–87].

Turning to the more practical feasibility tests, the LMB cells with both LFP and NMC811 cathodes, the former with the dual salt-based electrolyte exhibits higher specific capacities at 0.1C rate (Fig. S10). At 0.2C rate, the Li||LFP cells using single salt electrolytes undergo dramatic capacity fading, retaining less than 10 % after 200 cycles. In stark contrast, the dual salt electrolyte demonstrates a retention of ~93 % of the specific capacity of the 4th cycle and a CE of over 99 % across 200 cycles (Fig. 6a). The charge-discharge voltage profiles also show significantly lower polarization (Fig. 6b) as compared to the single salt electrolytes (Fig. S11).

The rate capability test shows the dual salt electrolyte cell to retain 58 % of its initial (0.1C) discharge capacity at 2C, in stark contrast to the single salt electrolyte cells' 5 % (Fig. 6c). Moreover, the CE is consistently high, ~98 % when back at 0.1C. The higher rate test (1C) renders *ca.* 86 % retained capacity after 500 cycles with a CE >99 % from the 4th

to the 500th cycle (Fig. 6d).

Turning to the LMB cells based on NMC811 the charge-discharge voltage profiles recorded at 0.1C rate show a steep potential rise to 3.97 V, followed by a drop to 3.89 V for the 1st cycle after delivering a capacity of 226.5 mAh g^{-1} (Fig. 7a), something previously attributed to a Li_2CO_3 layer being formed on the surface of the NMC811 particles, originating from moisture or air exposure. From the 2nd cycle and onwards the voltage profiles overlap, suggesting that CO_3^{2-} oxidation primarily occurs during the initial cycle [88–90]. Overall, the Li||NMC811 cell with the dual salt electrolyte exhibits a very good to excellent capacity retention of 90 %, with an average CE exceeding 98 % at 0.2C rate after 100 cycles (Fig. 7b).

The single salt electrolyte-based cells deliver lower capacities and capacity retentions (Figs. S12 and S13), while the cells with the dual salt electrolyte demonstrates lower polarization and more stable capacity even after 200 cycles (Fig. 7c), which by derivative plots (dQ/dV) show three reversible phase transformations corresponding to H1–M, M–H2, and H2–H3, indicating that the reversible phase transformations of NMC811 occurs consistently (Fig. 7d) [91,92]. The rate performance (Fig. S14) is comparable to that observed for the Li||LFP cell and in addition higher rate (1C) cycling demonstrates 88 % retained capacity after 500 cycles (Fig. 7e). The Nyquist plots for the data of the cell using the LiSac electrolyte show the interfacial resistance to initially be large but to decrease progressively during subsequent cycles. In contrast, the data for the LiBOB electrolyte based cell exhibits an increase in interfacial resistance after the 25th cycle, followed by a decrease, with dual semicircles appearing in the lower frequency region (Fig. S15). This suggests that the single salt electrolytes promote side reactions and lead to unstable interfacial layers being formed. In stark contrast, the dual salt electrolyte based cell data display minimal changes in the interfacial resistance over all 500 cycles, indicating formation of stable interfacial layers.

To get a somewhat deeper, yet mostly qualitative, insight into the role of the CEI for the performance, XPS analysis was conducted on the pristine and cycled NMC811 electrodes (Fig. 8). The analysis of the C 1s spectra areas reveals the presence of more organic components (C–O at ~285.8 eV and O–C=O at ~288.9 eV) in the CEI when using the single salt electrolytes, as compared to the pristine NMC electrode (Fig. S16) as well as to when using the dual salt electrolyte (Fig. 8). Furthermore, the O 1s spectra support this notion (Fig. S17) [93,94]. The B1s spectra show inorganic-rich layers attributed to Li–B–O and B_xO_y, suggesting that the BOB anion contributes to the formation of the CEI (Fig. 8d and e).

Moreover, the N 1s spectra display peaks corresponding to Li_3N, N–SO_x and $LiNO_2$, respectively (Fig. 8f and g) [95,96]. These species are generated by decomposition of the Sac anion. The S 2p spectra using the single salt LiSac-based and dual salt electrolytes indicate SO_3^{2-} and SO_4^{2-} contributing uniformly to the CEI formation (Fig. 8h and i) [95,97]. The SO_3^{2-} species is dominant using both single salt and dual salt electrolytes. Overall, the CEI formed when using the dual salt electrolyte is more inorganic and hence also more stable – in full agreement with the LMB literature.

4. Conclusions

The dual salt electrolyte demonstrates the physical and electrochemical properties desired for LMBs originating in that the combination of LiBOB with LiSac adjusts the cation coordination to favor anions and thereby improves the reduction stability of the electrolyte. It also enhances the lithium-ion transfer, cycling stability, rate performance and overall high-voltage LMB cell properties, *e.g.* the Li||NMC811 cells retained nearly the same specific capacity as Li||LFP cells after 500 cycles at the same current density. This is attributed to the formation of robust, inorganic-rich CEI, and this without relying on any LiF-based components. Overall, this is a significant stepping-stone towards the employment of fluorine-free electrolytes to create medium-to-high-voltage NMC811-based LMBs, even if the coin-cells made admittedly are not optimized in terms of electrolyte volume, electrode loading, cell balancing, *etc*.

CRediT authorship contribution statement

Ashok Kushwaha: Writing – review & editing, Writing – original draft, Methodology, Investigation, Formal analysis, Conceptualization. **Sayantika Bhakta:** Formal analysis. **Mukhtiar Ahmed:** Writing – review & editing, Formal analysis. **Andrei Filippov:** Writing – review & editing, Formal analysis. **Rong An:** Formal analysis. **Patrik Johansson:** Writing – review & editing. **Faiz Ullah Shah:** Writing – review & editing, Supervision, Resources, Project administration, Funding acquisition.

Declaration of competing interest

The authors declare that they have no known competing financial interests or personal relationships that could have appeared to influence the work reported in this paper.

Acknowledgements

The J. Gustaf Richert Foundation is gratefully acknowledged for the financial support in the form of a stipend for AK (Grant number: 2023-00824). The authors gratefully acknowledge the financial support from the Swedish Research Council for Sustainable Development (Grant number: 2020-00969), as well as the Swedish Research Council's (VR) Distinguished Professor grant 'Next Generation Batteries' (Grant number: 2021-00613) to PJ.

Appendix A. Supplementary data

Supplementary data to this article can be found online at https://doi.org/10.1016/j.jpowsour.2025.239241.

Data availability

Data will be made available on request.

References

[1] F. Degen, M. Winter, D. Bendig, J. Tübke, Energy consumption of current and future production of lithium-ion and post lithium-ion battery cells, Nat. Energy 8 (11) (2023) 1284–1295, https://doi.org/10.1038/s41560-023-01355-z.
[2] X.B. Cheng, R. Zhang, C.Z. Zhao, Q. Zhang, Toward safe lithium metal anode in rechargeable batteries: a review, Chem. Rev. 117 (2017) 10403–10473, https://doi.org/10.1021/acs.chemrev.7b00115.
[3] J. Xiao, Q. Li, Y. Bi, M. Cai, B. Dunn, T. Glossmann, J. Liu, T. Osaka, R. Sugiura, B. Wu, J. Yang, J.G. Zhang, M.S. Whittingham, Understanding and applying coulombic efficiency in lithium metal batteries, Nat. Energy 5 (8) (2020) 561–568, https://doi.org/10.1038/s41560-020-0648-z.
[4] B. Liu, J.G. Zhang, W. Xu, Advancing Lithium Metal Batteries, vol. 2, 2018, pp. 833–845, https://doi.org/10.1016/j.joule.2018.03.008.
[5] R. Konar, S. Maiti, B. Markovsky, H. Sclar, D. Aurbach, Exploring the capability of framework materials to improve cathodes' performance for high-energy lithium-ion batteries, Chem. Mater. 4 (2024) e2300039, https://doi.org/10.1002/cmtd.202300039.
[6] H. Zhang, Z. Zeng, S. Cheng, J. Xie, Recent progress and perspective on lithium metal battery with nickel-rich layered oxide cathode, eScience (2024) 100265, https://doi.org/10.1016/j.esci.2024.100265.
[7] Y. Zhao, T. Zhou, T. Ashirov, M. El Kazzi, C. Cancellieri, L.P.H. Jeurgens, J.W. Choi, A. Coskun, Fluorinated ether electrolyte with controlled solvation structure for high voltage lithium metal batteries, Nat. Commun. 13 (1) (2022) 2575, https://doi.org/10.1038/s41467-022-29199-3.
[8] T. Dong, S. Zhang, Z. Ren, L. Huang, G. Xu, T. Liu, S. Wang, G. Cui, Electrolyte engineering toward high performance high nickel (Ni ≥ 80%) lithium-ion batteries, Adv. Sci. 11 (2024) 2305753, https://doi.org/10.1002/advs.202305753.
[9] S. Ko, T. Obukata, T. Shimada, N. Takenaka, M. Nakayama, A. Yamada, Y. Yamada, Electrode potential influences the reversibility of lithium-metal anodes, Nat. Energy 7 (12) (2022) 1217–1224, https://doi.org/10.1038/s41560-022-01144-0.
[10] M.D. Tikekar, S. Choudhury, Z. Tu, L.A. Archer, Design principles for electrolytes and interfaces for stable lithium-metal batteries, Nat. Energy 1 (2016) 114, https://doi.org/10.1038/nenergy.2016.114.

[11] S. Kim, J.S. Kim, L. Miara, Y. Wang, S.K. Jung, S.Y. Park, Z. Song, H. Kim, M. Badding, J.M. Chang, V. Roev, G. Yoon, R. Kim, J.H. Kim, K. Yoon, D. Im, K. Kang, High-energy and durable lithium metal batteries using garnet-type solid electrolytes with tailored lithium-metal compatibility, Nat. Commun. 13 (1) (2022) 1883, https://doi.org/10.1038/s41467-022-29531-x.
[12] K.H. Park, Q. Bai, D.H. Kim, D.Y. Oh, Y. Zhu, Y. Mo, Y.S. Jung, Design strategies, practical considerations, and new solution processes of sulfide solid electrolytes for all-solid-state batteries, Adv. Energy Mater. 8 (18) (2018) 1800035, https://doi.org/10.1002/aenm.201800035.
[13] L. Fan, S. Wei, S. Li, Q. Li, Y. Lu, Recent progress of the solid-state electrolytes for high-energy metal-based batteries, Adv. Energy Mater. 16 (2018) 1702657, https://doi.org/10.1002/aenm.201702657.
[14] M. Zhang, H. Wang, A. Shao, Z. Wang, X. Tang, S. Li, J. Liu, Y. Ma, Enabling 4.5 V solid polymer batteries through a 10 Mm, crosslinked polyether electrolyte, Adv. Energy Mater. 14 (14) (2024) 2303932, https://doi.org/10.1002/aenm.202303932.
[15] Z.Y. Wang, C.Z. Zhao, S. Sun, Y.K. Liu, Z.X. Wang, S. Li, R. Zhang, H. Yuan, J. Q. Huang, Achieving high-energy and high-safety lithium metal batteries with high-voltage-stable solid electrolytes, Matter 6 (2023) 1096–1124, https://doi.org/10.1016/j.matt.2023.02.012. Cell Press.
[16] J. Janek, W.G. Zeier, Challenges in speeding up solid-state battery development, Nat. Energy 8 (2023) 230–240, https://doi.org/10.1038/s41560-023-01208-9.
[17] S. Li, F. Pei, Y. Ding, X. Guo, X. Zhang, H. Tao, Z. He, H. Hu, L. Zhang, Metal-organic framework-derived elastic solid polymer electrolytes enabled by covalent crosslinking for high-performance lithium metal batteries, Adv. Funct. Mater. 35 (7) (2025) 2415495, https://doi.org/10.1002/adfm.202415495.
[18] J. Yu, X. Lin, J. Liu, J.T.T. Yu, M.J. Robson, G. Zhou, H.M. Law, H. Wang, B. Z. Tang, F. Ciucci, In situ fabricated quasi-solid polymer electrolyte for high-energy-density lithium metal battery capable of subzero operation, Adv. Energy Mater. 12 (2) (2022) 2102932, https://doi.org/10.1002/aenm.202102932.
[19] J. Hu, C. Lai, K. Chen, Q. Wu, Y. Gu, C. Wu, C. Li, Dual fluorination of polymer electrolyte and conversion-type cathode for high-capacity all-solid-state lithium metal batteries, Nat. Commun. 13 (1) (2022) 7914, https://doi.org/10.1038/s41467-022-35636-0.
[20] Z. Zeng, V. Murugesan, K.S. Han, X. Jiang, Y. Cao, L. Xiao, X. Ai, H. Yang, J. G. Zhang, M.L. Sushko, J. Liu, Non-flammable electrolytes with high salt-to-solvent ratios for Li-Ion and Li-Metal batteries, Nat. Energy 3 (8) (2018) 674–681, https://doi.org/10.1038/s41560-018-0196-y.
[21] W. Mrozik, M.A. Rajaeifar, O. Heidrich, P. Christensen, Environmental impacts, pollution sources and pathways of spent lithium-ion batteries, Energy Environ. Sci. 14 (2021) 6099–6121, https://doi.org/10.1039/d1ee00691f.
[22] A. Capasso, A.E. Del Rio Castillo, H. Sun, A. Ansaldo, V. Pellegrini, F. Bonaccorso, Ink-jet printing of graphene for flexible electronics: an environmentally-friendly approach, Solid State Commun. 224 (2015) 53–63, https://doi.org/10.1016/j.ssc.2015.08.011.
[23] A.M. Li, O. Borodin, T.P. Pollard, W. Zhang, N. Zhang, S. Tan, F. Chen, C. Jayawardana, B.L. Lucht, E. Hu, X.Q. Yang, C. Wang, Methylation enables the use of fluorine-free ether electrolytes in high-voltage lithium metal batteries, Nat. Chem. 16 (6) (2024) 922–929, https://doi.org/10.1038/s41557-024-01497-x.
[24] K.S. Teoh, M. Melchiorre, S. Darlami Magar, M. Hermesdorf, D. Leistenschneider, M. Oschatz, F. Ruffo, J.L. Gómez Urbano, A. Balducci, Fluorine-free lithium-ion capacitor with enhanced sustainability and safety based on bio-based γ-Valerolactone and lithium Bis(Oxalato)Borate electrolyte, Adv. Mater. 36 (18) (2024) 2310056, https://doi.org/10.1002/adma.202310056.
[25] I.A. Khan, O.I. Gnezdilov, A. Filippov, F.U. Shah, Ion transport and electrochemical properties of fluorine-free lithium-ion battery electrolytes derived from biomass, ACS Sustain. Chem. Eng. 9 (23) (2021) 7769–7780, https://doi.org/10.1021/acssuschemeng.1c00939.
[26] O.I. Gnezdilov, A. Filippov, I. Ali Khan, F. Ullah Shah, Translational and reorientational dynamics of ionic liquid-based fluorine-free lithium-ion battery electrolytes, J. Mol. Liq. 345 (2022) 117001, https://doi.org/10.1016/j.molliq.2021.117001.
[27] F.U. Shah, O.I. Gnezdilov, I.A. Khan, A. Filippov, N.A. Slad, P. Johansson, Structural and ion dynamics in fluorine-free oligoether carboxylate ionic liquid-based electrolytes, J. Phys. Chem. B 124 (43) (2020) 9690–9700, https://doi.org/10.1021/acs.jpcb.0c04749.
[28] Y. Shuai, Y. Hu, X. Gong, Z. Xu, L. Li, L. Zhang, M. Li, J. Zhou, M. Li, Fluorine-free electrolytes for high-performance and low-cost lithium metal batteries, Chem. Eng. J. 505 (2025) 159101, https://doi.org/10.1016/j.cej.2024.159101.
[29] T.D. Pham, A. Bin Faheem, J. Kim, K. Kwak, K.K. Lee, Non-flammable electrolytes based on a fluorine-free salt for safe and high-voltage lithium metal batteries, Electrochim. Acta 458 (2023) 142496, https://doi.org/10.1016/j.electacta.2023.142496.
[30] G. Hernández, R. Mogensen, R. Younesi, J. Mindemark, Fluorine-free electrolytes for lithium and sodium batteries, Batteries and Supercaps 5 (2022) e202100373, https://doi.org/10.1002/batt.202100373.
[31] L. Jiang, C. Liang, H. Li, Q. Wang, J. Sun, Safer triethyl-phosphate-based electrolyte enables nonflammable and high-temperature endurance for a lithium ion battery, ACS Appl. Energy Mater. 3 (2) (2020) 1719–1729, https://doi.org/10.1021/acsaem.9b02188.
[32] G.T. Kim, S.S. Jeong, M. Joost, E. Rocca, M. Winter, S. Passerini, A. Balducci, Use of natural binders and ionic liquid electrolytes for greener and safer lithium-ion batteries, J. Power Sources 196 (4) (2011) 2187–2194, https://doi.org/10.1016/j.jpowsour.2010.09.080.
[33] T. Yong, J. Wang, Y. Mai, X. Zhao, H. Luo, L. Zhang, Organosilicon compounds containing nitrile and Oligo(Ethylene oxide) substituents as safe electrolytes for high-voltage lithium-ion batteries, J. Power Sources 254 (2014) 29–32, https://doi.org/10.1016/j.jpowsour.2013.12.087.
[34] X. Zhou, D. Peng, K. Deng, H. Chen, H. Zhou, J. Wang, Synthesis and characterization of novel fluorinated nitriles as non-flammable and high-voltage electrolytes for Lithium/lithium-ion batteries, J. Power Sources 557 (2023) 232557, https://doi.org/10.1016/j.jpowsour.2022.232557.
[35] X. Wang, C. Yamada, H. Naito, G. Segami, K. Kibe, High-concentration trimethyl phosphate-based nonflammable electrolytes with improved charge–discharge performance of a graphite anode for lithium-ion cells, J. Electrochem. Soc. 153 (1) (2006) A135, https://doi.org/10.1149/1.2136078.
[36] Z. Ni, C. Wei, Z. Wang, Y. Li, X. Zhang, S. Xiong, J. Feng, Tri-anions regulated solvation structure in intrinsically nonflammable phosphate-based electrolytes for stable lithium metal batteries, Energy Storage Mater. 71 (2024) 103603, https://doi.org/10.1016/j.ensm.2024.103603.
[37] X. Yang, Z. Zeng, M. Liu, S. Wang, C. Li, M. Qin, J. Xie, Multidentate ether modifies solvation structure in nonflammable phosphate electrolytes for wide-temperature lithium-ion batteries, Commun. Chem. 8 (1) (2025) 179, https://doi.org/10.1038/s42004-025-01562-7.
[38] K. Xu, B. Deveney, K. Nechev, Y. Lam, T.R. Jow, Evaluating LiBOB/Lactone electrolytes in large-format lithium-ion cells based on nickelate and iron phosphate, J. Electrochem. Soc. 155 (12) (2008) 2990708, https://doi.org/10.1149/1.2990708. A959.
[39] I. Phiri, J. Kim, D.H. Oh, M. Ravi, H.S. Bae, J. Hong, S. Kim, Y.C. Jeong, Y.M. Lee, Y.G. Lee, M.H. Ryou, Synergistic effect of a dual-salt liquid electrolyte with a LiNO3Functional additive toward stabilizing thin-film Li metal electrodes for Li secondary batteries, ACS Appl. Mater. Interfaces 13 (27) (2021) 31605–31613, https://doi.org/10.1021/acsami.1c04972.
[40] C. Farina, L. Bernard, M. Landa, N. Leconte, L. Picard, A novel fluorine-free lithium salt derived from malononitrile for electrolyte applications in liquid and solid-state batteries, Electrochim. Acta 525 (2025) 146183, https://doi.org/10.1016/j.electacta.2025.146183.
[41] H. Zhang, X. Judez, A. Santiago, M. Martinez-Ibañez, M.Á. Muñoz-Márquez, J. Carrasco, C. Li, G.G. Eshetu, M. Armand, Fluorine-free noble salt anion for high-performance all-solid-state lithium–sulfur batteries, Adv. Energy Mater. 9 (25) (2019) 1900763, https://doi.org/10.1002/aenm.201900763.
[42] N. Karimi, M. Zarrabeitia, A. Mariani, D. Gatti, A. Varzi, S. Passerini, Nonfluorinated ionic liquid electrolytes for lithium metal batteries: ionic conduction, electrochemistry, and interphase formation, Adv. Energy Mater. 11 (4) (2021) 2003521, https://doi.org/10.1002/aenm.202003521.
[43] F.A. Kreth, L. Köps, C. Leibing, S. Darlami Magar, M. Hermesdorf, K. Schutjajew, C. Neumann, D. Leistenschneider, A. Turchanin, M. Oschatz, J.L. Gómez Urbano, A. Balducci, Enabling fluorine-free lithium-ion capacitors and lithium-ion batteries for high-temperature applications by the implementation of lithium Bis(Oxalato) Borate and ethyl isopropyl sulfone as electrolyte, Adv. Energy Mater. 14 (13) (2024) 2303909, https://doi.org/10.1002/aenm.202303909.
[44] K. Xu, S. Zhang, T.R. Jow, W. Xu, C.A. Angell, LiBOB as salt for lithium-ion batteries. A possible solution for high temperature operation, Electrochem. Solid State Lett. 5 (1) (2002) 1426042, https://doi.org/10.1149/1.1426042.
[45] J. Li, J. Yang, Z. Ji, M. Su, H. Li, Y. Wu, X. Su, Z. Zhang, Prospective application, mechanism, and deficiency of lithium Bis(Oxalate)Borate as the electrolyte additive for lithium-batteries, Adv. Energy Mater. 13 (2023) 2301422, https://doi.org/10.1002/aenm.202301422.
[46] Y. Li, W. Li, R. Shimizu, D. Cheng, H.N. Nguyen, J. Paulsen, S. Kumakura, M. Zhang, Y.S. Meng, Elucidating the effect of borate additive in high-voltage electrolyte for Li-Rich layered oxide materials, Adv. Energy Mater. 12 (11) (2022) 2103033, https://doi.org/10.1002/aenm.202103033.
[47] M. Klein, M. Binder, M. Koželj, A. Perini, T. Gouveia, T. Diemant, A. Schür, S. Brutti, E. Bodo, D. Bresser, J.L. Gómez-Urbano, A. Balducci, Understanding the role of imide-based salts and borate-based additives for safe and high-performance glyoxal-based electrolytes in Ni-Rich NMC811 cathodes for Li-Ion batteries, Small 20 (2024) 2401610, https://doi.org/10.1002/smll.202401610.
[48] L. Yang, M.M. Furczon, A. Xiao, B.L. Lucht, Z. Zhang, D.P. Abraham, Effect of impurities and moisture on lithium bisoxalatoborate (LiBOB) electrolyte performance in lithium-ion cells, J. Power Sources 195 (6) (2010) 1698–1705, https://doi.org/10.1016/j.jpowsour.2009.09.056.
[49] M. Ahmed, A. Kushwaha, A. Filippov, P. Johansson, F. Ullah Shah, Saccharinate-based ionic liquids and lithium battery electrolytes, Batter Supercaps 8 (2025) e202400758, https://doi.org/10.1002/batt.202400758.
[50] O. Borodin, W. Gorecki, G.D. Smith, M. Armand, Molecular dynamics simulation and pulsed-field gradient NMR studies of Bis(Fluorosulfonyl)Imide (FSI) and Bis [(Trifluoromethyl)Sulfonyl]Imide (TFSI)-based ionic liquids, J. Phys. Chem. B 114 (20) (2010) 6786–6798, https://doi.org/10.1021/jp911950q.
[51] H. Matsumoto, Physical and electrochemical properties of room temperature molten salt based on aliphatic onium cations and asymmetric amide anion, ECS Proceedings Volumes 2002–19 (1) (2002) 1057–1065, https://doi.org/10.1149/200219.1057pv.
[52] Z. Wen, W. Fang, F. Wang, H. Kang, S. Zhao, S. Guo, G. Chen, Dual-salt electrolyte additive enables high moisture tolerance and favorable electric double layer for lithium metal battery, Angew. Chem., Int. Ed. 63 (13) (2024) 2314876, https://doi.org/10.1002/anie.202314876.
[53] Y. Li, F. Ding, Y. Shao, H. Wang, X. Guo, C. Liu, X. Sui, G. Sun, J. Zhou, Z. Wang, Solvation structure and derived interphase tuning for high-voltage Ni-Rich lithium metal batteries with high safety using gem-difluorinated ionic liquid based dual-salt electrolytes, Angew. Chem., Int. Ed. 63 (8) (2024) 2317148, https://doi.org/10.1002/anie.202317148.

[54] H. Zheng, H. Xiang, F. Jiang, Y. Liu, Y. Sun, X. Liang, Y. Feng, Y. Yu, Lithium difluorophosphate-based dual-salt low concentration electrolytes for lithium metal batteries, Adv. Energy Mater. 10 (30) (2020) 2001440, https://doi.org/10.1002/aenm.202001440.
[55] R. Miao, J. Yang, X. Feng, H. Jia, J. Wang, Y. Nuli, Novel dual-salts electrolyte solution for dendrite-free lithium-metal based rechargeable batteries with high cycle reversibility, J. Power Sources 271 (2014) 291–297, https://doi.org/10.1016/j.jpowsour.2014.08.011.
[56] B. Jiang, H. Xu, X. Cheng, J. Li, H. Wang, Y. Liu, Dual-salt electrolyte with synergistic effect for lithium metal batteries with prolonging cyclic performance, Chemelectrochem 9 (2) (2022) 2101251, https://doi.org/10.1002/celc.202101251.
[57] L. El Ouatani, R. Dedryvère, C. Siret, P. Biensan, S. Reynaud, P. Iratçabal, D. Gonbeau, The effect of vinylene carbonate additive on surface film formation on both electrodes in Li-Ion batteries, J. Electrochem. Soc. 156 (2) (2009) A103, https://doi.org/10.1149/1.3029674.
[58] L. Chen, K. Wang, X. Xie, J. Xie, Effect of Vinylene Carbonate (VC) as Electrolyte Additive on Electrochemical Performance of Si Film Anode for Lithium Ion Batteries, J. Power Sources 174 (2) (2007) 538–543, https://doi.org/10.1016/j.jpowsour.2007.06.149.
[59] T. Frömling, M. Kunze, M. Schönhoff, J. Sundermeyer, B. Roling, Enhanced lithium transference numbers in ionic liquid electrolytes, J. Phys. Chem. B 112 (41) (2008) 12985–12990, https://doi.org/10.1021/jp804097j.
[60] M. Gouverneur, J. Kopp, L. Van Wüllen, M. Schönhoff, Direct determination of ionic transference numbers in ionic liquids by electrophoretic NMR, Phys. Chem. Chem. Phys. 17 (45) (2015) 30680–30686, https://doi.org/10.1039/c5cp05753a.
[61] J. Evans, C.A. Vincent, P.G. Bruce, Electrochemical measurement of transference numbers in polymer electrolytes, Polymer 28 (1987) 2324.
[62] K.M. Abraham, Z. Jiang, B. Carroll, Highly conductive PEO-like polymer electrolytes, Chem. Mater. 9 (1997) 1978–1988.
[63] H. Chen, K. Chen, L. Luo, X. Liu, Z. Wang, A. Zhao, H. Li, X. Ai, Y. Fang, Y. Cao, LiNO3-Based electrolytes via electron-donation modulation for sustainable nonaqueous lithium rechargeable batteries, Angew. Chem., Int. Ed. 63 (10) (2024) 2316966, https://doi.org/10.1002/anie.202316966.
[64] Y. Li, W. Li, R. Shimizu, D. Cheng, H.N. Nguyen, J. Paulsen, S. Kumakura, M. Zhang, Y.S. Meng, Elucidating the effect of borate additive in high-voltage electrolyte for Li-Rich layered oxide materials, Adv. Energy Mater. 12 (11) (2022) 2103033, https://doi.org/10.1002/aenm.202103033.
[65] F. Årén, R. Andersson, A.A. Franco, P. Johansson, Global and local structure of lithium battery electrolytes: origin and onset of highly concentrated electrolyte behavior, J. Electrochem. Soc. 170 (6) (2023) 060506, https://doi.org/10.1149/1945-7111/acd8f9.
[66] R. Andersson, F. Årén, A.A. Franco, P. Johansson, Ion transport mechanisms via time-dependent local structure and dynamics in highly concentrated electrolytes, J. Electrochem. Soc. 167 (14) (2020) 140537, https://doi.org/10.1149/1945-7111/abc657.
[67] G.V. Zhuang, K. Xu, T.R. Jow, P.N. Ross, Study of SEI layer formed on graphite anodes in PC/LiBOB electrolyte using IR spectroscopy, Electrochem. Solid State Lett. 7 (8) (2004), https://doi.org/10.1149/1.1756855.
[68] R. Holomb, W. Xu, H. Markusson, P. Johansson, P. Jacobsson, Vibrational spectroscopy and Ab initio studies of lithium Bis(Oxalato)Borate (LiBOB) in different solvents, J. Phys. Chem. A 110 (40) (2006) 11467–11472, https://doi.org/10.1021/jp0626824.
[69] F.U. Shah, A. Holmgren, M.W. Rutland, S. Glavatskih, O.N. Antzutkin, Interfacial behavior of orthoborate ionic liquids at inorganic oxide surfaces probed by NMR, IR, and Raman spectroscopy, J. Phys. Chem. C 122 (34) (2018) 19687–19698, https://doi.org/10.1021/acs.jpcc.8b06049.
[70] Y.C. Lee, C.W. Liew, M.H. Buraidah, H.J. Woo, Fourier transform infrared studies of gel polymer electrolyte based on Poly(Acrylamide-Co-Acrylic acid) – ethylene carbonate incorporated with water-soluble sodium sulfide, Opt. Mater. 140 (2023), https://doi.org/10.1016/j.optmat.2023.113791.
[71] S. Bhowmick, M. Ahmed, A. Filippov, L.C. Loaiza, F.U. Shah, P. Johansson, Ambient temperature liquid salt electrolytes, Chem. Commun. 59 (18) (2023) 2620–2623, https://doi.org/10.1039/d3cc00318c.
[72] Y.H. Feng, M. Liu, W. Qi, H. Liu, Q. Liu, C. Yang, Y. Tang, X. Zhu, S. Sun, Y.M. Li, T. L. Chen, B. Xiao, X. Ji, Y. You, P.F. Wang, Dual-anionic coordination manipulation induces phosphorus and boron-rich gradient interphase towards stable and safe sodium metal batteries, Angewandte Chemie int 64 (2024) e20241564, https://doi.org/10.1002/anie.202415644.
[73] K. Chen, X. Shen, L. Luo, H. Chen, R. Cao, X. Feng, W. Chen, Y. Fang, Y. Cao, Correlating the solvating power of solvents with the strength of ion-dipole interaction in electrolytes of lithium-ion batteries, Angew. Chem., Int. Ed. 62 (47) (2023) 2312373, https://doi.org/10.1002/anie.202312373.
[74] A. Guéguen, D. Streich, M. He, M. Mendez, F.F. Chesneau, P. Novák, E.J. Berg, Decomposition of LiPF 6 in high energy lithium-ion batteries studied with online electrochemical mass spectrometry, J. Electrochem. Soc. 163 (6) (2016) A1095–A1100, https://doi.org/10.1149/2.0981606jes.
[75] T. Ma, G.L. Xu, Y. Li, L. Wang, X. He, J. Zheng, J. Liu, M.H. Engelhard, P. Zapol, L. A. Curtiss, J. Jorne, K. Amine, Z. Chen, Revisiting the corrosion of the aluminum current collector in lithium-ion batteries, J. Phys. Chem. Lett. 8 (5) (2017) 1072–1077, https://doi.org/10.1021/acs.jpclett.6b02933.
[76] X. Zhang, B. Winget, M. Doeff, J.W. Evans, T.M. Devine, Corrosion of aluminum current collectors in lithium-ion batteries with electrolytes containing LiPF[Sub 6], J. Electrochem. Soc. 152 (11) (2005) 41867, https://doi.org/10.1149/1.2041867. B448.
[77] A. Kushwaha, A. Sharma, B.B. Bhatt, A. Mukhopadhyay, D. Gupta, Inkjet-printed graphene-modified aluminum current collector for high-voltage lithium-ion battery, ACS Appl. Energy Mater. 6 (8) (2023) 4168–4178, https://doi.org/10.1021/acsaem.2c03870.
[78] X. Zhang, T.M. Devine, Passivation of aluminum in lithium-ion battery electrolytes with LiBOB, J. Electrochem. Soc. 153 (9) (2006) 18269, https://doi.org/10.1149/1.2218269. B365.
[79] H.A. Ishfaq, C. Cruz Cardona, E. Tchernychova, P. Johansson, R. Dominko, S. Drvarič Talian, Enhanced performance of lithium metal batteries via cyclic fluorinated ether based electrolytes, Energy Storage Mater. 69 (2024) 103375, https://doi.org/10.1016/j.ensm.2024.103375.
[80] F. Wu, A. Mullaliu, T. Diemant, D. Stepien, T.N. Parac-Vogt, J.K. Kim, D. Bresser, G. T. Kim, S. Passerini, Beneficial impact of lithium Bis(Oxalato)Borate as electrolyte additive for high-voltage nickel-rich lithium-battery cathodes, InfoMat 5 (8) (2023) 12462, https://doi.org/10.1002/inf2.12462.
[81] J.H. Um, S.H. Yu, Unraveling the mechanisms of lithium metal plating/stripping via in situ/operando analytical techniques, Adv. Energy Mater. 11 (2021) 2003004, https://doi.org/10.1002/aenm.202003004.
[82] N.W. Li, Y.X. Yin, J.Y. Li, C.H. Zhang, Y.G. Guo, Passivation of lithium metal anode via hybrid ionic liquid electrolyte toward stable Li plating/stripping, Adv. Sci. 4 (2) (2017) 1600400, https://doi.org/10.1002/advs.201600400.
[83] M. Petzl, M.A. Danzer, Nondestructive detection, characterization, and quantification of lithium plating in commercial lithium-ion batteries, J. Power Sources 254 (2014) 80–87, https://doi.org/10.1016/j.jpowsour.2013.12.060.
[84] S. Tan, O. Borodin, N. Wang, D. Yen, C. Weiland, E. Hu, Synergistic anion and solvent-derived interphases enable lithium-ion batteries under extreme conditions, J. Am. Chem. Soc. 146 (44) (2024) 30104–30116, https://doi.org/10.1021/jacs.4c07806.
[85] N. Chen, M. Feng, C. Li, Y. Shang, Y. Ma, J. Zhang, Y. Li, G. Chen, F. Wu, R. Chen, Anion-dominated conventional-concentrations electrolyte to improve low-temperature performance of lithium-ion batteries, Adv. Funct. Mater. 34 (33) (2024) 2400337, https://doi.org/10.1002/adfm.202400337.
[86] J. Lee, W. Choi, E. Jang, H. Kim, J. Yoo, Dual-anion ionic liquid electrolytes: a strategy for achieving high stability and conductivity in lithium metal batteries, Energy Environ. Sci. 18 (2025) 5277–5286, https://doi.org/10.1039/d5ee00119f.
[87] H. Zheng, H. Xiang, F. Jiang, Y. Liu, Y. Sun, X. Liang, Y. Feng, Y. Yu, Lithium difluorophosphate-based dual-salt low concentration electrolytes for lithium metal batteries, Adv. Energy Mater. 10 (30) (2020) 2001440, https://doi.org/10.1002/aenm.202001440.
[88] X. Li, J. Liu, J. He, H. Wang, S. Qi, D. Wu, J. Huang, F. Li, W. Hu, J. Ma, Hexafluoroisopropyl trifluoromethanesulfonate-driven easily Li+ desolvated electrolyte to afford Li||NCM811 cells with efficient anode/cathode electrolyte interphases, Adv. Funct. Mater. 31 (37) (2021) 2104395, https://doi.org/10.1002/adfm.202104395.
[89] H. Liu, A.J. Naylor, A.S. Menon, W.R. Brant, K. Edström, R. Younesi, Understanding the roles of Tris(Trimethylsilyl) phosphite (TMSPi) in LiNi0.8Mn0.1Co0.1O2 (NMC811)/Silicon–Graphite (Si–Gr) lithium-ion batteries, Adv. Mater. Interfac. 7 (15) (2020) 2000277, https://doi.org/10.1002/admi.202000277.
[90] W. Li, Z. He, Y. Jie, F. Huang, Y. Chen, Y. Wang, W. Zhang, X. Zhu, R. Cao, S. Jiao, Understanding and design of cathode–electrolyte interphase in high-voltage lithium–metal batteries, Adv. Funct. Mater. 5 (2024) 202406770, https://doi.org/10.1002/adfm.202406770.
[91] S. Kim, J.H. Jeon, K. Park, S.H. Kweon, J.H. Hyun, C. Song, D. Lee, G. Song, S. H. Yu, T.K. Lee, S.K. Kwak, K.T. Lee, S.Y. Hong, N.S. Choi, Electrolyte design for high-voltage lithium-metal batteries with synthetic sulfonamide-based solvent and electrochemically active additives, Adv. Mater. 36 (24) (2024) 202401615, https://doi.org/10.1002/adma.202401615.
[92] S. Zheng, C. Hong, X. Guan, Y. Xiang, X. Liu, G.L. Xu, R. Liu, G. Zhong, F. Zheng, Y. Li, X. Zhang, Y. Ren, Z. Chen, K. Amine, Y. Yang, Correlation between long range and local structural changes in Ni-Rich layered materials during charge and discharge process, J. Power Sources 412 (2019) 336–343, https://doi.org/10.1016/j.jpowsour.2018.11.053.
[93] Y. Lu, Q. Cao, W. Zhang, T. Zeng, Y. Ou, S. Yan, H. Liu, X. Song, H. Zhou, W. Hou, P. Zhou, N. Hu, Q. Feng, Y. Li, K. Liu, Breaking the molecular symmetricity of sulfonimide anions for high-performance lithium metal batteries under extreme cycling conditions, Nat. Energy 10 (2024) 191–204, https://doi.org/10.1038/s41560-024-01679-4.
[94] T. Deng, X. Fan, L. Cao, J. Chen, S. Hou, X. Ji, L. Chen, S. Li, X. Zhou, E. Hu, D. Su, X.Q. Yang, C. Wang, Designing in-situ-formed interphases enables highly reversible cobalt-free LiNiO2 cathode for Li-Ion and Li-Metal batteries, Joule 3 (10) (2019) 2550–2564, https://doi.org/10.1016/j.joule.2019.08.004.
[95] Y. Li, M. Liu, K. Wang, C. Li, Y. Lu, A. Choudhary, T. Ottley, D. Bedrov, L. Xing, W. Li, Single-solvent-based electrolyte enabling a high-voltage lithium-metal battery with long cycle life, Adv. Energy Mater. 13 (2023) 202300918, https://doi.org/10.1002/aenm.202300918.
[96] X. Li, J. Zheng, M.H. Engelhard, D. Mei, Q. Li, S. Jiao, N. Liu, W. Zhao, J.G. Zhang, W. Xu, Effects of imide-orthoborate dual-salt mixtures in organic carbonate electrolytes on the stability of lithium metal batteries, ACS Appl. Mater. Interfaces 10 (3) (2018) 2469–2479, https://doi.org/10.1021/acsami.7b15117.
[97] J.Y. Wei, X.Q. Zhang, L.P. Hou, P. Shi, B.Q. Li, Y. Xiao, C. Yan, H. Yuan, J. Q. Huang, Shielding polysulfide intermediates by an organosulfur-containing solid electrolyte interphase on the lithium anode in lithium–sulfur batteries, Adv. Mater. 32 (2020) 2003012, https://doi.org/10.1002/adma.202003012.